Magnetic Purcell enhancement by plasmon-induced magnetic resonance of the nanoparticle-on-mirror configuration

Ze Li,[1,*,†] Yafei Li,[1,*] Qingzhang You,[2] Meng Wang,[1] Chengjun Zhu,[1] Yuxing Yang,[1] Hongmei Luan,[1] and Peijie Wang[2,‡]

[1]*Key Laboratory of Semiconductor Photovoltaic Technology and Energy Materials of Inner Mongolia Autonomous Region, School of Physical Science and Technology, Inner Mongolia University, Hohhot 010021, People's Republic of China*

[2]*The Beijing Key Laboratory for Nano-Photonics and Nano-Structure, Department of Physics, Capital Normal University, Beijing 100048, People's Republic of China*

(Received 24 March 2024; revised 3 June 2024; accepted 18 June 2024; published 19 July 2024)

We theoretically reveal that plasmonic nanocavities with 1 nm gaps between the nanosphere and gold film support multiple resonances possessing ultrahigh-field confinement and enhancements for both the electric and magnetic fields. Here, a circulated electric line supported by the plasmonic mode implies that a magnetic dipole is introduced in the center of the gap region. A high magnetic enhancement factor of up to 100 is observed, and multipolar expansion demonstrates that symmetry breaking suppresses the radiation of the dipole mode. The surface charges accumulate in the gap area and form the electric-quadrupole (**Qe**) mode and magnetic-dipole (**m**) modes in the gap region, and then the interference between the dominant **Qe** and **m** modes gives rise to a pronounced magnetic-based Fano resonance in the scattering spectrum, thus boosting the magnetic response in the scattering valley. Next, we introduce a magnetic dipole in the gap region, where a significant radiative magnetic Purcell factor of up to 200 is observed, following the Fano valley of the scattering spectrum. Furthermore, the ultrasmall magnetic mode volume and high magnetic field at the Fano valley frequencies demonstrate this phenomenon. This study unlocks new possibilities for single-photon emission from the magnetic-dipole transition in the nanoparticle-on-mirror configuration.

DOI: 10.1103/PhysRevA.110.013516

I. INTRODUCTION

Light-matter interaction is the core issue of light research, and in the past decade, the main focus of light-matter interaction has been the interaction between matter and the electric field of light; because the component of the magnetic field is several orders of magnitude weaker than the electric field, the interaction of matter with a magnetic field is not always considered. Only some electronic transitions exhibit a significant "magnetic-dipole" character, implying that they couple to the magnetic field of light [1–6]. Similar to the Purcell effect on electric-dipole transitions, magnetic-dipole transitions can be manipulated by the local density of optical states (LDOS) (magnetic Purcell effect) [5,6]. The modification of the LDOS and manipulation of magnetic-dipole transitions has been studied in metallic mirrors and plasmonic arrays [5–8]. However, a low LDOS limits the emission enhancement of magnetic-dipole emitters [5–9]. According to the Purcell factor, the spontaneous emission of a magnetic dipole can be modified by a magnetic near field [6]. The Mie-resonance-based dielectric nanostructure exhibits magnetic multipolar resonance at optical frequencies and has been suggested as a viable platform for enhancing magnetic-dipole transitions [10–15]. The localized electromagnetic (EM) fields generated in the Mie resonator are mostly concentrated in the particle interior [14–18], which implies that they are difficult to access and interact with; thus a low enhancement factor was observed (less than 100) [18,19].

Metallic nanoresonators can trap light in a subwavelength volume via the collective excitation of localized surface plasmons [20]. As the most representative nanoresonator, the metallic nanoparticle-on-mirror (NPOM) configuration can enhance, confine, and manipulate light in the single-emitter or molecule level [20,21]. Importantly, the possibility of tuning the resonance wavelength by modifying the gap region makes it possible to use NPOM over a broad optical frequency range. Compared to the prototypical dimer system [22,23], the gap region between the nanoparticle and substrate mirror is more controllable, and gaps with nanometer or even subnanometer precision can be easily achieved by the assembly of molecular layers [22,24], atomic layer deposition [25], or shell-isolated techniques [26]. The extreme limitations of EM fields in the gap of (NPOM) resonators offer broad applications including light-matter strong coupling [24], plasmon-enhanced spectroscopy [21–23,27,28], and nonlinear effects [26].

Although NPOM provides a powerful platform for modifying the LDOS, it also enhances the decay rate of the electric-dipole transitions of fluorescent emitters [21–23]. However, there have been few reports of Purcell enhancement by manipulating magnetic-dipole transitions in NPOM; once the effective magnetic Purcell enhancement happens in the NPOM construct, the corresponding magnetic resonance "hot spots" must be induced in the gap region [28]. Recently,

*These authors contributed equally to this work.
†Contact author: li@imu.edu.cn
‡Contact author: pjwang@cnu.edu.cn

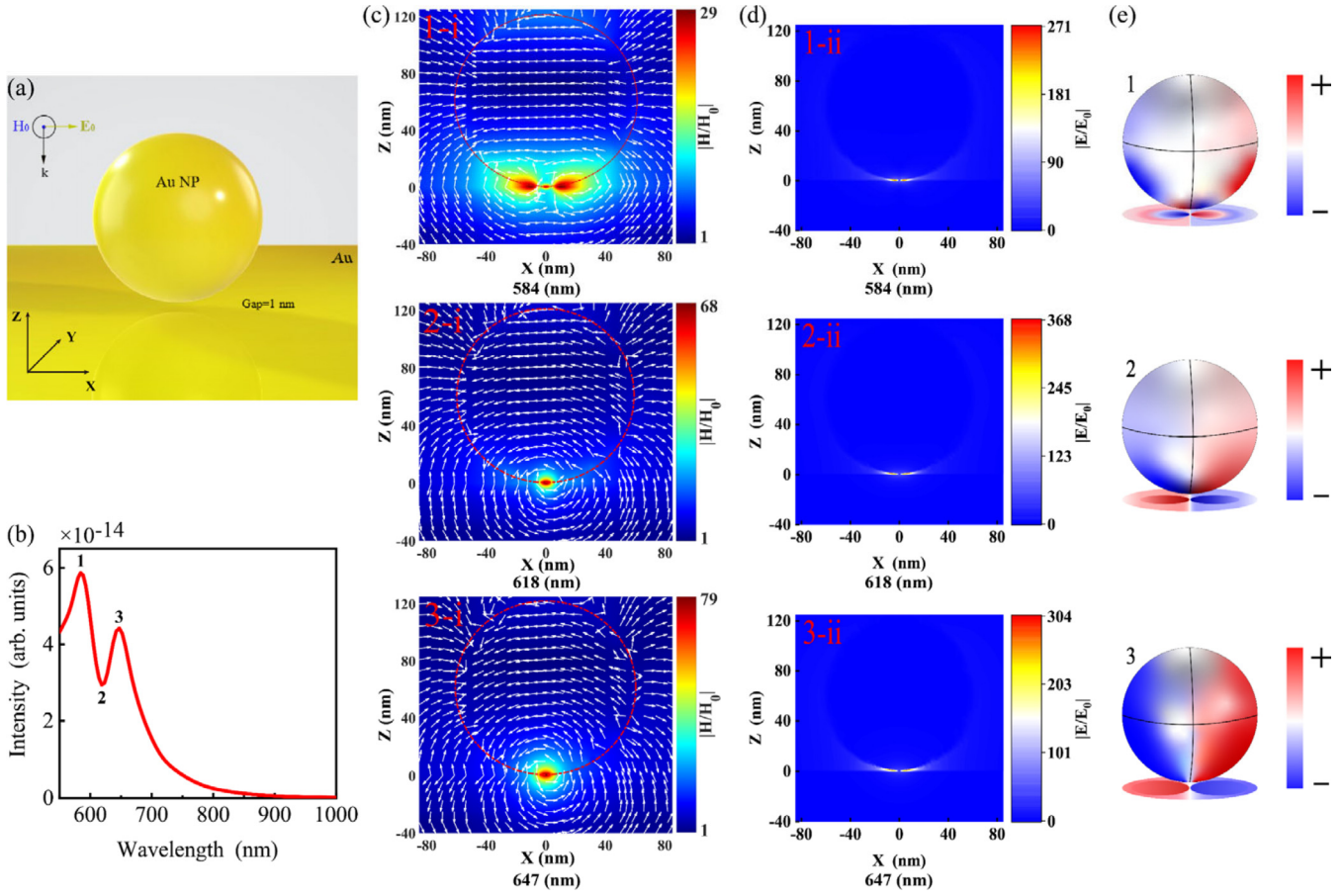

FIG. 1. (a) Schematic of the studied nanoparticle on mirror (NPOM). The size of the nanosphere and the gap between the nanosphere and the gold film are set at 120 and 1 nm, respectively. The polarization of light is along the z axis and the magnetic field is along the y axis. (b) Simulated far-field scattering spectrum of the NPOM system corresponding to the structure of (a); the two scattering peaks and scattering valley are labeled 1, 2, and 3, respectively. Electric displacement vectors superimposed with magnetic-field H distribution in the XZ plane [(c-1-i), (c-2-i), (c-3-i)] and the pure electric-field E distribution [(d-1-ii), (d-2-ii), (d-3-ii)] corresponding to the labels 1, 2, and 3 in the scattering spectrum of 1(b). Here, the magnetic nature of this mode is evident on inspection of the calculated circulating electric-field distribution. (e) Three-dimensional charge distribution corresponding to the two peak wavelengths and valley wavelength, marked as 1 (584 nm), 2 (618 nm), and 3 (647 nm), of the NPOM system in (a).

several investigations have theoretically demonstrated that the magnetic hot spot resonance can be induced in different plasmon nanoparticle platforms including multiple nanoparticle systems and NPOM constructs [28–36]. This research shows significant potential for the study of magnetic Purcell enhancement in NPOM configurations.

In this study, we first demonstrate that a magnetic-dipolar mode can be induced in the gap of a NPOM system due to the interference between the dominant **Qe** and **m** modes, which give rise to a pronounced magnetic-based Fano resonance in the scattering spectrum. Further, we introduce magnetic dipoles and systematically investigate the radiative magnetic Purcell enhancement under magnetic-dipolar resonance in the NPOM system. We find that the radiative magnetic Purcell enhancement is a function of the nanosphere radius, and is inversely proportional to the mode volume, reaching a maximum enhancement factor of up to 255, which is comparable to the radiative magnetic Purcell factor of the isotropic magnetic dipole in a Si nanocavity [37].

II. RESULTS AND DISCUSSION

Figure 1 shows a typical example of a magnetic-resonance-supported NPOM configuration, which can be experimentally constructed by simply assembling gold nanospheres on a gold substrate; the gap between the nanosphere and the gold film is 1 nm, which can be achieved by depositing a molecular layer. Nanospheres with diameters of 70–200 nm can be prepared by wet chemistry synthesis in actual experiments [28]. When this nanostructure is illuminated by the z-polarized light with magnetic field H in the y direction, a strong scattering band with two peaks at 584 and 647 nm and a scattering valley at 618 nm is observed in Fig. 1(b). Here, the valley between two peaks is actually Fano resonance caused by mode interference between the subradiative magnetic-dipole moment and the superradiative electric multipole moment [28,32,38–40].

To verify the essence of magnetic-based Fano resonance, we present near-field distributions that include magnetic field H superimposed with the electric-field lines [Fig. 1(c)],

electric fields [Fig. 1(d)], and surface charges [Fig. 1(e)] at three selected wavelengths marked "1" (scattering peak 584 nm) and "3" (scattering peak 647 nm), and the scattering valley marked "2" (618 nm).

First, we focus on the near field in Fig. 1(c-2-i) at the scattering valley of 618 nm. Apparently, the circulating electric-field line distribution (white arrows) forms a loop that is correlated with the magnetic field concentrated in its center, which implies the generation of the magnetic-dipole resonance in the center of the gap region. Here, this excited magnetic-dipolar moment is parallel with the incident magnetic field. It should be noted that the physical nature of the magnetic mode is the plasmon-induced magnetic mode (PIMR). A further examination of the corresponding electric field and the electric charge distribution reveals the coupling nature of the magnetic-dipole mode. In Fig. 1(d-2-ii), the electric field is mainly concentrated at the gap edges of the magnetic region, so the three-dimensional (3D) surface-charge distributions in Fig. 1(e-2) show most of the surface charge is induced within the small gap region. Meanwhile the antiphase charge distribution characteristic on the bottom of the real sphere and imaging mirror is induced, indicating this excited electric quadrupole may be responsible for the magnetic-based Fano resonance features in Fig. 1(c-2-i).

Second, we also investigate near-field properties corresponding to two scattering peaks at 584 and 647 nm wavelengths (marked 1 and 2). For the second peak (647 nm), electric [Fig. 1(d-3-ii)] and magnetic responses [Fig. 1(c-3-i)] similar to the result of the scattering valley (618 nm). However, the (3D) surface-charge distributions in Fig. 1(e-3) demonstrate more surface-charge distributions on the left and right nanosphere surfaces, instead of near the nanogap, intensifying and behaving like an electric dipole. Meanwhile, these features that are confirmed by the magnetic and electric near field of the scattering valley are more localized than that of the scattering peak. Because of the stronger electric response, this mode corresponds to an intermediate state between the electric and magnetic-dipole modes.

For the first peak (584 nm), as evidenced by (a) electric-field lines filling magnetic-field [Fig. 1(c-1-i)], (b) electric-field distribution [Fig. 1(d-1-ii)], and (c) surface-charge distributions [Fig. 1(e-1)], this new mode can be regarded as belonging to a higher gap-plasmon mode.

It is worth noting that the effective magnetic-based optical Fano resonance strongly depends on the geometric symmetry of the nanocavity. Usually, to induce unnatural magnetic-dipole (MD) resonances in plasmonic structures, more than three nanoparticles need to be closely clustered with a nanometer gap [30,36,38–40], which requires the excitation of a dipole moment in a single nanoparticle, and then multiple dipole moments on each individual nanosphere are connected end to end to form a closed electric-field loop, resulting in the manifestation of a magnetic dipole [30,38–41] (Appendix E). Furthermore, the introduction of the structure symmetry breaking will cause the radiation suppression of the total electric-dipole moment and boost the magnetic dipole; then the interference between the electric-dipole (**p**) and magnetic-dipole (**m**) modes gives rise to a pronounced a magnetic-based Fano resonance in the scattering spectrum [38,39]. Obviously, the above statement cannot support the generation mechanism of magnetic-based Fano resonance in the NPOM structure.

And as we all know, the nanoparticle-on-a-mirror (NPOM) construct can be considered as an analog of a real nanoparticle dimer consisting of two identical nanospheres [42]. Therefore, in order to gain a deeper understanding the magnetic-based Fano response in the scattering spectrum caused by symmetry breaking, we employ the multipolar expansion method to quantitatively analyze the far-field contribution of different electromagnetic modes in nanosphere dimers with different symmetries, composed of Au nanospheres of different sizes.

The different moments in the multipole decomposition were computed from the calculated distribution of polarization current inside the nanoparticle $\mathbf{J} = -i\omega\mathbf{P} = -i\omega\varepsilon_0(\varepsilon_r - 1)\mathbf{E}(\mathbf{r})$, where $\mathbf{P}$ is the polarization vector, ω is the angular frequency, ε_0 is the permittivity of vacuum and ε_r the relative permittivity of nanoparticle, and $\mathbf{E}(\mathbf{r})$ is the electric field induced by the incident light wave inside the nanoparticle [38,43,44].

For a nonmagnetic medium, the multipole moment contributions to the far-field radiation including the electric dipole $\mathbf{p}_\alpha$, magnetic dipole $\mathbf{m}_\alpha$, and the electric quadrupole $\mathbf{Q}^{\mathbf{e}}_{\alpha\beta}$ and magnetic quadrupole $\mathbf{Q}^{\mathbf{m}}_{\alpha\beta}$ can be derived as [38,43–46]

$$\mathrm{ED}: \mathbf{p}_\alpha = -\frac{1}{i\omega}\left\{\int d^3\mathbf{r}\mathbf{J}^\omega_\alpha j_0(kr) + \frac{k^2}{2}\int d^3\mathbf{r}\left[3(\mathbf{r}\cdot\mathbf{J}_\omega)r_\alpha - r^2\mathbf{J}^\omega_\alpha\right]\frac{j_{2(kr)}}{(kr)^2}\right\}, \quad (1)$$

$$\mathrm{MD}: \mathbf{m}_\alpha = \frac{3}{2}\int d^3\mathbf{r}(\mathbf{r}\times\mathbf{J}_\omega)_\alpha\frac{j_1(kr)}{kr}, \quad (2)$$

$$\mathrm{EQ}: \mathbf{Q}^{\mathbf{e}}_{\alpha\beta} = -\frac{3}{i\omega}\left\{\int d^3\mathbf{r}\left[3\left(r_\beta\mathrm{J}^\omega_\alpha + r_\alpha\mathrm{J}^\omega_\beta\right) - 2(\mathbf{r}\cdot\mathbf{J}_\omega)\delta_{\alpha\beta}\right]\times\frac{j_1(kr)}{kr} + 2k^2\int d^3\mathbf{r}[5r_\alpha r_\beta(\mathbf{r}\cdot\mathbf{J}_\omega) - (r_\alpha\mathrm{J}_\beta + r_\alpha J_\beta)r^2 - r^2(\mathbf{r}\cdot\mathbf{J}_\omega)\delta_{\alpha\beta}]\frac{j_{3(kr)}}{(kr)}^3\right\}, \quad (3)$$

$$\mathrm{MQ}: \mathbf{Q}^{\mathbf{m}}_{\alpha\beta} = 15\int d^3\mathbf{r}\{r_\alpha(\mathbf{r}\times\mathbf{J}_\omega)_\beta + r_\beta(\mathbf{r}\times\mathbf{J}_\omega)_\alpha\}\frac{j_2(kr)}{(kr)^2}, \quad (4)$$

where $\mathbf{p}_\alpha$, $\mathbf{m}_\alpha$, $\mathbf{Q}^{\mathbf{e}}_{\alpha\beta}$, and $\mathbf{Q}^{\mathbf{m}}_{\alpha\beta}$ are the spherical multipole moments expressed in the Cartesian coordinates, $\alpha, \beta = x, y, z$.

Next, the relative radiated powers from each multipole are [47]

$$I^p = \frac{2\omega^4}{3c^3}|\mathbf{p}_\alpha|^2, \quad (5)$$

$$I^m = \frac{2\omega^4}{3c^3}|\mathbf{m}_\alpha|^2, \quad (6)$$

$$I^{\mathrm{Qe}} = \frac{\omega^6}{5c^5}\left|\mathbf{Q}^{\mathbf{e}}_{\alpha\beta}\right|^2, \quad (7)$$

$$I^{\mathrm{Qm}} = \frac{\omega^6}{20c^5}\left|\mathbf{Q}^{\mathbf{m}}_{\alpha\beta}\right|^2, \quad (8)$$

$$I^{\mathrm{total}} = I^p + I^m + I^{\mathrm{Qe}} + I^{\mathrm{Qm}}. \quad (9)$$

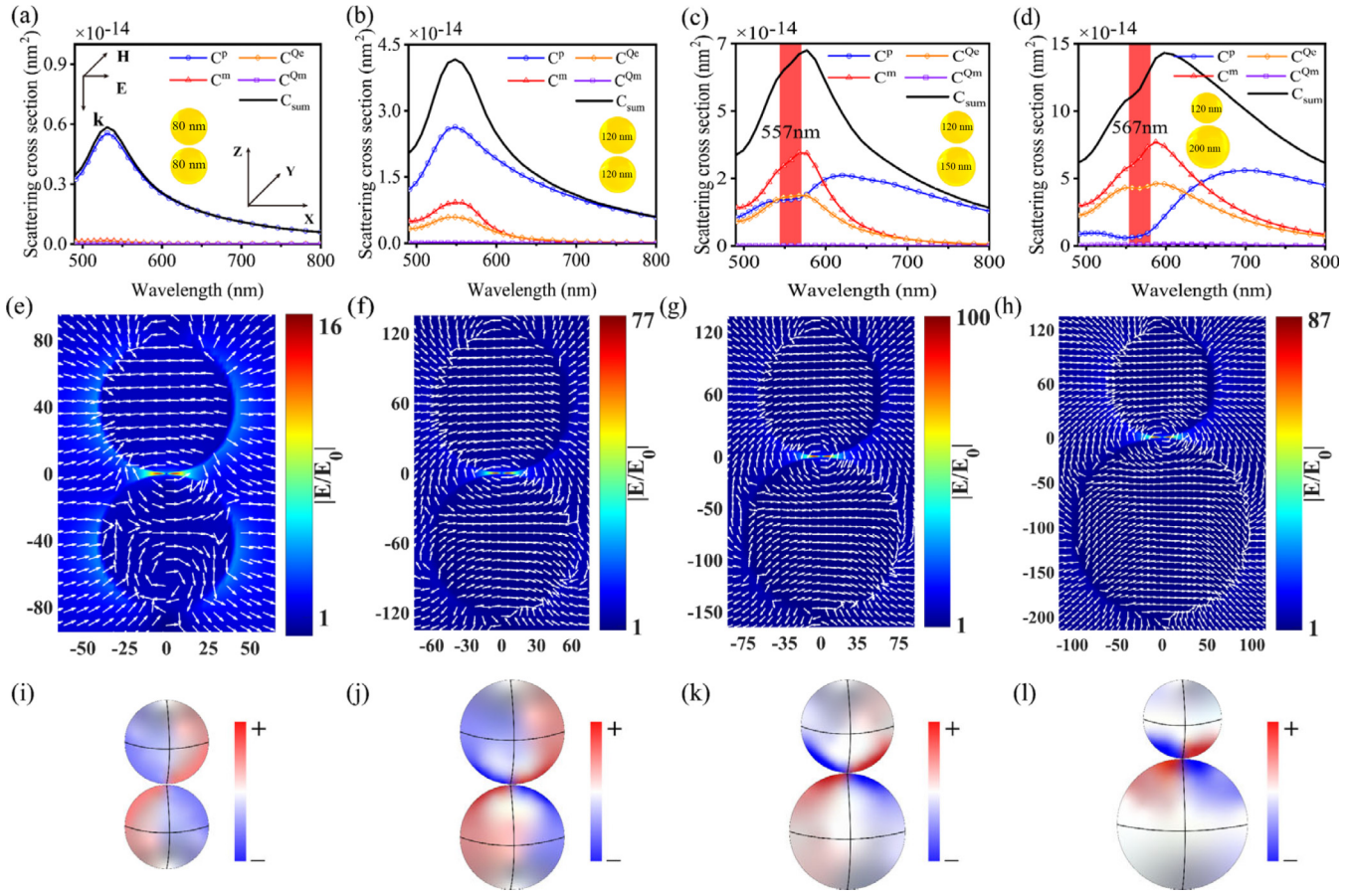

FIG. 2. (a)–(d) Simulated scattering cross sections and the multipole expansion of the symmetric nanosphere dimer with uniform diameter ($D1 = D2$) and asymmetric nanosphere dimer ($D1 \neq D2$). The size of the nanosphere is shown inside and the gap size was set constant at 1 nm for all cases. (e,f) Electric displacement vector superimposed with electric-field distribution in the XZ plane calculated at the peak wavelength of C_{sum} curves corresponding to 530 nm (e) and 548 nm (f), and (g), (h) the Fano dip wavelength (marked with red line) corresponding to 557 nm (g) and 567 nm (h), respectively. (i)–(l) Three-dimensional charge distribution map corresponding to (e)–(h).

Finally, the scattering cross-section contribution from each multipole (c^p, c^m, c^{Qe}, c^{Qm}) is obtained by normalizing to the incident power density. Then the total scattering cross section of the nanoparticle system can be obtained by summing the scattering cross section from each multipole [43,44]:

$$\begin{aligned} C_{\text{sca}}^{\text{total}} &= C_{\text{sca}}^{p} + C_{\text{sca}}^{m} + C_{\text{sca}}^{\text{Qe}} + C_{\text{sca}}^{\text{Qm}} \\ &= \frac{k^4}{6\pi\varepsilon_0^2|\mathbf{E}_0|^2}\left[\sum_{\alpha}\left(|p_\alpha|^2 + \frac{|m_\alpha|^2}{c}\right)\right. \\ &\quad \left. + \frac{1}{120}\sum_{\alpha\beta}\left(\left|kQ_{\alpha\beta}^{e}\right|^2 + \left|\frac{kQ_{\alpha\beta}^{m}}{c}\right|^2\right)\right], \end{aligned} \tag{10}$$

where $|\mathbf{E}_0|$ is the electric-field amplitude of the incident light, k is the wave number, and c is the speed of light.

We started multipole decomposition with the symmetric nanosphere dimer. Figures 2(a) and 2(b) show the calculated scattering power for all multipole modes of the symmetric nanosphere dimer with uniform diameter ($D1 = D2$) 80 and 120 nm; here the gap size is set to 1 nm. When illuminated with the same plane wave in Fig. 1, for the smaller symmetric nanosphere dimer ($D = 80$ nm), only the electric-dipole (**p**) mode was excited at 530 nm [Figs. 2(e) and 2(i)]; the magnetic dipole (**m**) and the electric quadrupole (**Qe**) were not excited. For the symmetric geometry with a diameter of 120 nm, we observed that the **p** mode still dominates in the scattering power, and also the **m** mode is excited in the scattering peak; although both the electric and magnetic responses are excited simultaneously, they are completely uncoupled [38,41], and the corresponding electric-field line distribution [Fig. 2(f)] and the 3D charge distribution [Fig. 2(j)] in the scattering peak also demonstrate this feature. Next, the asymmetric condition is introduced. Figure 2(c) shows the scattering spectrum of the asymmetric nanosphere dimer ($D1 = 120$ nm and $D2 = 150$ nm); despite the relatively small differences in the diameter of $D2$, the simulated scattering spectrum is remarkably different. Here, two main features can be clearly seen: (i) a small Fano dip at 557 nm (marked with red line) is observed in the total field scattering spectrum ($\mathbf{C_{sum}}$) and a considerable suppression of the electric-dipole mode (**p**) also appears at the same wavelength. Notably, the magnetic-dipole and electric-quadrupole contribution dominate at the resonance frequency, which can be explained in the induced surface-charge distribution results in Fig. 2(k); compared to the symmetric configuration in Fig. 2(j), the corresponding dipole electric charge at the left and right ends of the nanosphere is reduced in Fig. 2(k), and more induced surface charge is concentrated in

the gap region. Meanwhile, the induced electric dipole in the bottom of the nanosphere will couple to its image charge in the $D2$ sphere; this coupling then generates a quadrupolelike charge distribution, and the induced circulating displacement current supports a magnetic resonance in the same frequency range [28]. The electric-field line distribution in Figs. 2(g) and 2(h) also demonstrates that a pure magnetic-dipolar mode was formed in the gap region with the introduction of the asymmetry condition. (ii) As the diameter of $D2$ increases to 200 nm, the degree of symmetry destruction increases; as shown in Fig. 2(d), the Fano dip of the total scattering cross section is vivid at a wavelength of 567 nm [Fig. 2(d)]. At this wavelength, the dominant magnetic (C^m) and quadrupole C^{Qe} component still occurs, but the C^{Qe} experiences a drop, and at the wavelength of the Fano dip (567 nm), the scattering contribution of the electric-dipole mode is almost zero. So we deduce the symmetry breaking induces interference between **Qe** and the magnetic-dipole modes, which give rise to a pronounced Fano resonance in the scattering spectrum of the dimer. Moreover, as the diameter increases to 250 nm, this feature is more pronounced, as depicted in Fig. 7 in Appendix D. Furthermore, we found the wavelength of the Fano dip redshift with the degree of symmetry destruction increased. Once the diameter $D2$ becomes infinite, the dimer configuration becomes the NPOM structure; the corresponding spectrum response is shown in Fig. 1(b), which creates a pronounced Fano dip (618 nm) in the total scattering cross section. Thus multipolar decomposition demonstrates symmetry destruction, effectively boosting its magnetic Fano response in the scattering spectrum of Fig. 1(b) [38–40].

Meanwhile, our multipolar expansion analysis in Fig. 2 shows that the electric quadrupole scattering intensity contribution is crucial in both the symmetric and asymmetric configurations. This feature is related to our approach to realize the magnetic-dipole mode in the NPOM or the dimer configurations; it is necessary to form a closed electric-field loop in the gap area of the dual nanoparticles, so that the electric quadrupole moment must be excited in the gap region (Appendix E).

We also notice that compared to the magnetic modes in dimers or NPOM construct (Appendix E), the volume of the magnetic hot spot modes in polymers is relatively larger and the magnetic-field intensity is smaller $|H/H_0| = 16$, which is not conducive to conducting research on the interaction between the magnetic part of light and matter [30,31,33–36,38]. The normalized magnitude of magnetic-field distributions in Figs. 1(c-2-i) and 1(c-3-i) indicates that the strongest magnetic-field enhancement reaches as high as 68- and 79-fold of H_0 for the scattering valley and second peak wavelength, respectively. Therefore, the present NPOM configuration may open up new possibilities for the single-photon emission enhancement of magnetic-dipole transitions.

Here, we study spontaneous emission from a magnetic emitter characterized by a given magnetic-dipole moment with magnetic-field polarization along the y axis, which models the magnetic-dipolar transition moment of a fluorescent molecule in vacuum [19,48]. The emitter without intrinsic losses was set at the center of the gap region (0.5 nm above the substrate), which is the position of the magnetic local density of optical states (MLDOS) maxima. Figure 3(a) shows the far-field radiative decay rate (Γ_{rad}) of a magnetic-dipole emitter in the presence of the PIMR resonator normalized by the decay rate in vacuum (Γ_0) (details are in Appendix F). Near the Fano dip wavelength (618 nm), the significant enhancement factor reaches 180 at the center of the gap, which is better than the reported result for the magnetic Mie mode of the dielectric nanosphere. Figure 3(b) shows the electric field and electric-field line distributions excited by the magnetic-dipole emitters at this wavelength. Notably, the circulating electric line in the gap region is excited, which implies that the magnetic-dipole moment emitter couples with the magnetic-dipole resonance of the NPOM. Here, we also present the spectra of the radiative decay rate enhancement ($\Gamma_{\mathrm{rad}}/\Gamma_0$) for the magnetic-dipole emitter with gap distance of 1, 1.5, 2, 2.5, and 3 nm in Fig. 3(c). The emitters are positioned in the gap center of the NPOM system, and we observe that the magnetic Purcell factor decreases as the gap distance increases because the smallest gap distance is maintained at high magnetic LDOS and the smallest magnetic mode volume.

The black line in Fig. 3(d) shows the far-field radiation pattern at the wavelength of the magnetic resonance scattering valley of the bare NPOM system, and its radiating main lobe is confined mainly within the angle of -30° to 30° along the Z direction. The red line in Fig. 3(d) shows the emission pattern of the magnetic emitters corresponding to the emission peak in Fig. 3(a) (black line). Notably, the radiation lobes (black and red lines) are almost overlapped, which implies the emission from the magnetic emitter within the nanoscale plasmonic gaps depends on the PIMR mode, and the contributions from other plasmonic modes is negligible.

Furthermore, when we move the magnetic dipole to the locations of $X = 0$, 2, 4, 6.5, 8, 10, 20 nm for $y = 0$ nm, we find that the effective radiative magnetic Purcell factor is also excited, indicating that our approach is more conducive to practical applications and does not depend on the precise position of the molecules in the gap.

We now return to the PIMR structure and investigate the spectral shifts caused by variations in the nanosphere radius. The color map in Fig. 4(a) shows the scattering spectrum redshifts and the corresponding scattering section increases with the diameter; the dashed white, black, and red lines indicate the positions of the first peak, scattering valley, and second peak, respectively, which demonstrates the tuning ability of the PIMR mode based on the NPOM configuration. Therefore, finally, we explore the relationship between the magnetic Purcell factor and the size of the nanoparticle on a mirror. Figure 4(b) shows the magnetic radiative Purcell factor for a magnetic dipole in the center gap region as a function of the diameter of the nanosphere. The maximum magnetic Purcell factor follows the evolution trend of the scattering valley corresponding to the black dashed line in Fig. 4(a) and increases with the nanosphere diameter.

In this paper, for an emitter that is in the EM environment, the modified far-field radiation rate is proportional to the electromagnetic local photon density of states (EMLDOS) and inversely proportional to the mode volume V: $\Gamma_{\mathrm{rad}}/\Gamma_0 \propto \rho/V$. Specifically, the magnetic LDOS inside the nanocavity is approximately proportional to the magnetic-field intensities in Fig. 4(b) and is written as $\rho_H \propto |H_y|$. The H-field mode

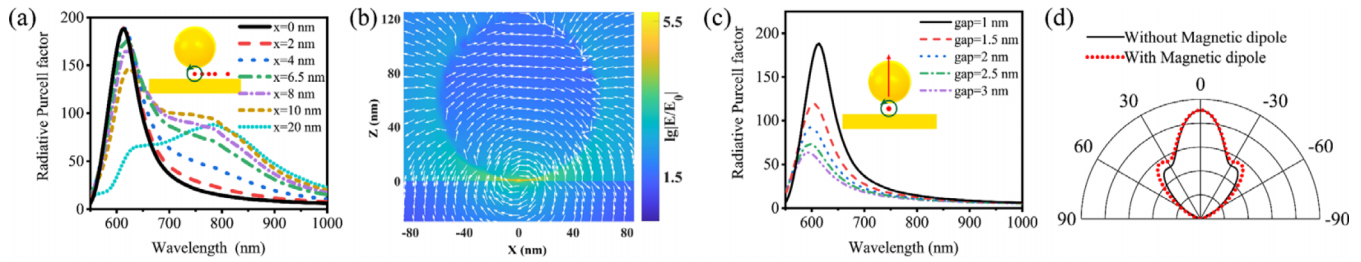

FIG. 3. Spontaneous emission of a magnetic-dipole emitter at the NPOM gap region. (a) The normalized far-field radiative decay rate (Γ_{rad}/Γ_0) of a magnetic-dipole emitter in the PIMR resonator varies with the relative position X of the magnetic dipole along the x direction. $X = 0$ denotes the center of the gap region. (b) Electric displacement vector representing electric-field distribution in the XZ plane excited at the peak wavelength (618 nm) in (a) $X = 0$ nm black line. (c) Normalized radiative decay rate (Γ_{rad}/Γ_0) spectra of the magnetic-dipole emitter at the center of the gap in the NPOM system varies with gap distance. (d) The normalized far-field radiation pattern in the XZ plane at the wavelength of PIMR mode (618 nm) with or without magnetic dipoles in the gap center of the NPOM system.

volume V of NPOM is calculated as follows:

$$V = \frac{\int H^2 dV^2}{\int H^4 dV}. \tag{11}$$

Figure 4(c) shows the corresponding H-field intensity in the center of the NPOM gap region. As expected, the maximum magnetic-field intensity follows the evolution trend of the scattering valley corresponding to the black solid line in Fig. 4(a). However, the increasing trend of the magnetic-field intensity is not sufficient to guarantee the enhancement of the magnetic factor; therefore, the corresponding magnetic mode volume in the scattering valley is calculated as Fig. 4(d). The magnetic mode volume is even smaller than the reported electric-field mode volume in Refs. [24,49]. Furthermore, as the diameter of the sphere increases, the mode volume of the magnetic dipole decreases, which explains why the volume of the nanosphere increases and the corresponding magnetic Purcell factor increases.

III. CONCLUSION

We demonstrate that the NPOM nanocavites between the nanosphere and mirror substrate support magnetic-based Fano resonance that possess ultrahigh magnetic-field enhancement. We perform multipole decomposition on the dimer resonator to highlight the interference between the dominant magnetic dipole and the **Qe** mode caused by symmetry-breaking conditions, which result in significant magnetic-based Fano resonance in the scattering spectrum.

Next, we introduce a magnetic dipole in the gap region and observe a significant radiative magnetic Purcell factor following the Fano valley of the scattering spectrum. Furthermore, we demonstrate that the ability of the PIMR resonator to confine the magnetic field of light to ultracompressed dimensions is pivotal for the strong magnetic Purcell effect in metallic nanoparticles. The PIMR of the NPOM configuration overlaps with the magnetic-dipole transition ($^5D_0 - ^7F_1$) of the rare earth ion Eu^{3+} at 590 nm [8,9]; we believe that our research has enormous potential for single-photon emission from emitters of magnetic-dipole transition. This may also result in entirely new applications of the NPOM configuration.

ACKNOWLEDGMENTS

The authors acknowledge the financial support by National Natural Science Foundation of China (Grants No. 12304339, No. 62265014, No. 62005134, and No. 62104120), the Inner Mongolia University 2022 High Level Talent Launch Project (Grant No. 10000-22311201/037), and the 2022 Autonomous Region level introduction of high-level talent research support (Grant No. 12000-15042237).

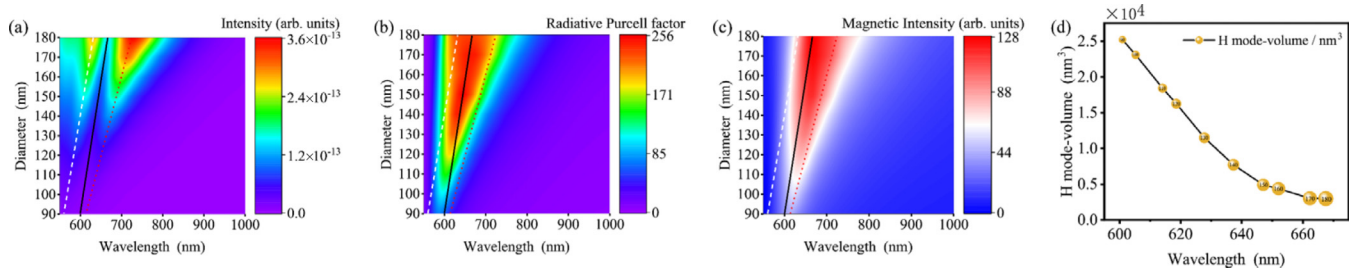

FIG. 4. Spectral shift caused by the change in the nanosphere radius. (a) Color map of the scattering spectra of the NPOM system as a function of the nanosphere diameter. The white dotted, black solid, and red dotted lines indicate the locations of the first scattering peak, scattering valley, and second scattering peak, respectively. (b) Color map of the magnetic radiative Purcell factor corresponding to the magnetic dipole in the central gap region of the NPOM system as a function of the nanosphere diameter. (c) The corresponding H-field intensity evolution of (a) at the center of the NPOM gap region. (d) The magnetic model volume at the wavelength of the PIMR scattering valley for different diameters of nanosphere.

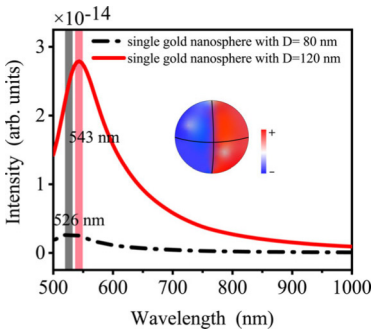

FIG. 5. Scattering spectrum of a single nanosphere.

APPENDIX A: NUMERICAL SIMULATIONS

We used LUMERICAL FDTD (finite difference time domain) SIMULATION to calculate the far-field and near-field optical magnetic response of the NPOM and dimer construct. The permittivity of gold was taken from the empirical data given by Johnson and Christy [50]. In simulations, a total-field scattered-field source acts as a linearly polarized light normally incident on the nanosphere or the substrate, and a closed monitor consisting of six discrete Fourier transform (DFT) monitors was added in the scattered-field region to measure total scattering cross sections in simulation. For the purpose of estimating the influence of oblique incidence on focused plasmonic modes, we theoretically compared deviations of scattering spectra under different incident angles of 0°, 10°, 20°, and 33°. Perfectly matched layer boundary conditions were adopted in order to avoid unphysical reflections around structures. The simulation time was set to 1000 fs, which sufficiently warranted the convergence. For computation-time saving, a nonuniform mesh method was generated. For the narrow gap region, 0.25 nm × 0.25 nm × 0.25 nm Yee cell size was set, whereas 1 nm × 1 nm × 1 nm was used in other regions. The surface-charge density is calculated from the Gauss's law $\rho = \varepsilon_0 \nabla \cdot \mathbf{E}$. For the multipole decomposition of a dimer, a 3D DFT monitor was utilized together with a 3D index monitor that has the same dimension to capture the electric-field distributions.

APPENDIX B: SCATTERING SPECTRA OF A SINGLE NANOSPHERE

For an independent gold nanosphere with diameter 80 or 120 nm, a broad resonant peak of the simulated scattering spectrum is centered at 526 and 543 nm, respectively. This scattering peak originates from the electric-dipole mode generated on the left and right nanosphere surfaces (see the inset in Fig. 5).

APPENDIX C: SCATTERING SPECTRA OF NPOM UNDER DIFFERENT INCIDENT ANGLES

To further verify the simulation results, we also calculated the scattering spectrum under different incident angles of 10°, 20°, and 30°, and the electric field is not parallel to the substrate, as shown in Fig. 6. We obtained similar scattering spectrum results, and the **E**-field line distribution at the valley at 30° also demonstrates the excitation of the magnetic mode;

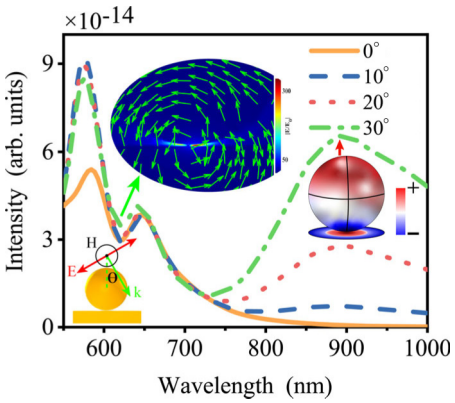

FIG. 6. Scattering spectrum of NPOM in Fig. 1 under different incident angles.

the broad peak at 900 nm is the vertical dipole moment. In all cases, two resonance peaks and a Fano valley was observed; deviations on focused electric and magnetic modes at the nanogap can be neglected.

APPENDIX D: MULTIPOLE DECOMPOSITION OF A MORE ASYMMETRIC DIMER

See Fig. 7. At the wavelength of the Fano dip (577 nm), the scattering contribution of the electric-dipole mode is completely zero; the dominant magnetic (C^{m}) and quadrupole (C^{Qe}) components still occurred. Therefore the symmetry breaking induces interference between Qe and magnetic-dipole modes, which give rise to a pronounced Fano resonance in the scattering spectrum of the dimer.

APPENDIX E: COMPARISON OF MAGNETIC MODES FORMED BY MULTIMERS AND DIMER OR NPOM CONSTRUCT

See Fig. 8. Usually, to induce unnatural magnetic-dipole (MD) resonances in plasmonic structure, more than three nanoparticles need to be closely clustered with a nanometer gap [30,36,38–40], which requires the excitation of a dipole moment in a single nanoparticle, and then multiple dipole moments on each individual nanosphere are connected

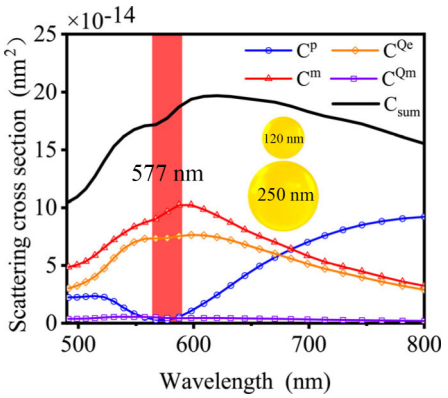

FIG. 7. Multipole decomposition of the asymmetric dimer with $D1 = 150$ nm and $D2 = 250$ nm.

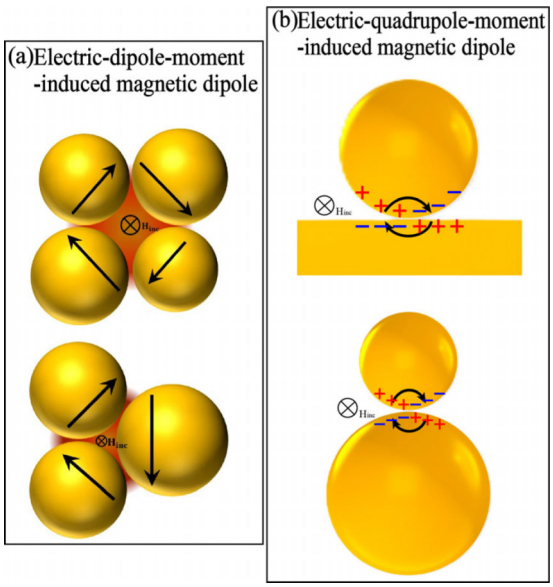

FIG. 8. The comparison of formation mechanisms of magnetic mode by multimer and dimer or NPOM construct.

end-to-end to form a closed electric-field loop, resulting in the manifestation of a magnetic dipole in the common gaps of multiple nanoparticles. However, compared to the magnetic modes in dimers or NPOM construct, the volume of the magnetic hot spot modes in polymers is larger and the magnetic-field intensity is smaller.

APPENDIX F: RADIATIVE MAGNETIC PURCELL EFFECT

The first proposal to modify spontaneous emission came in 1946 by Purcell, who suggested that nuclear magnetic transition rates could be increased by coupling the system to an electrical circuit resonator [51].

Usually, for an emitter that is not in free space, its modified emission rate is described by Fermi's "golden rule" as below [52],

$$\Gamma_g = \frac{2\pi}{\hbar^2}\sum_f |\langle f|H_I|i\rangle|^2\delta(\omega_i - \omega_f), \tag{F1}$$

with the initial state $|i\rangle$, and the final state $|f\rangle$. The interaction Hamiltonian H_I can be described as

$$H = -p\cdot E - m\cdot B, \tag{F2}$$

$$\Gamma_g = \frac{\pi\omega}{3\hbar}\left[\varepsilon_0^{-1}|\mathbf{p}|^2\rho_E(r,\omega) + \mu_0|\mathbf{m}|^2\rho_B(r,\omega)\right]. \tag{F3}$$

$\mathbf{p}$ is the electric and $\mathbf{m}$ is the magnetic-dipole moment of the emitter. In this paper, we focus on the problem of magnetic-dipole emission. Thus, the electric part can be neglected and

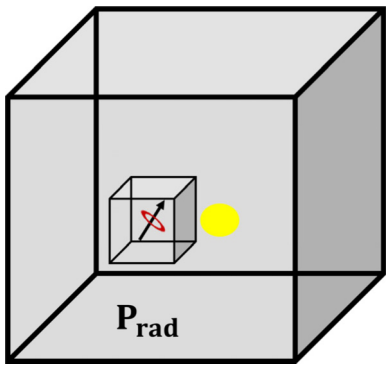

FIG. 9. Illustration of the surfaces used to calculate the power radiated to the far field P_{rad}.

it is convenient to rewrite as [52,53]

$$\Gamma_g = \frac{\pi\omega}{3\hbar}[\mu_0|\mathbf{m}|^2\rho_B(r,\omega)], \tag{F4}$$

where $\rho_B(r,\omega)$ is the magnetic LDOS, which is proportional to the magnetic intensity at the position of the magnetic dipole.

The original Purcell factor always is defined as $F_P = \frac{\Gamma_g}{\Gamma_0} = \frac{3Q\lambda^3}{4\pi^2 V_0}$; Γ_0 is the spontaneous emission rate of magnetic moment transitions in free space. λ is the wavelength associated with the transition, Q is the quality factor of the cavity mode, and V_0 is its volume.

The Purcell factor correctly includes radiative as well as nonradiative decay channels; our paper focuses only on the radiative Purcell factor, the radiative part of the total Purcell effect F_P, and we call the radiative (Γ_{rad}) rate enhancement as the radiative Purcell factor F_{rad}. Usually in simulation, the radiative Purcell factor is described by the equations

$$F_{\text{rad}} = \frac{\Gamma_{\text{rad}}}{\Gamma_0} = \frac{P_{\text{rad}}}{P_0} = \frac{P_{\text{tot}}}{P_0} - \frac{P_{\text{abs}}}{P_0}, \tag{F5}$$

where P_{tot} and P_0 are the total powers emitted by the magnetic dipole with and without the optical nanostructures, respectively. P_{rad} is the power radiated in the far field in the presence of the optical cavity. P_{abs} is the power absorbed by the cavity. See Fig. 9.

In FDTD simulation, a localized magnetic emitter can be modeled as an oscillating current source with $P_0 = \omega^4|\mu|^2/12\pi\varepsilon_0 c^3$. To compute P_{rad} with FDTD, one closed surface monitor consisting of six DFT monitors was added around the entire system (nanoparticle and emitter), as illustrated in Fig. 9, where $P_{\text{rad}} = \int_{\sum} s\cdot nds$ can then be determined by integrating the calculated Poynting vector s over the surface monitor; n is the normal to the surface $\sum$. These popular computational methods are also used and recommended in Refs. [19,21,23,37,54].

[1] S. Karaveli and R. Zia, Spectral tuning by selective enhancement of electric and magnetic dipole emission, Phys. Rev. Lett. **106**, 193004 (2011).

[2] L. Aigouy, A. Caze, P. Gredin, M. Mortier, and R. Carminati, Mapping and quantifying electric and magnetic dipole luminescence at the nanoscale, Phys. Rev. Lett. **113**, 076101 (2014).

[3] T. H. Taminiau, S. Karaveli, N. F. van Hulst, and R. Zia, Quantifying the magnetic nature of light emission, Nat. Commun. **3**, 979 (2012).

[4] M. Kasperczyk, S. Person, D. Ananias, L. D. Carlos, and L. Novotny, Excitation of magnetic dipole transitions at optical frequencies, Phys. Rev. Lett. **114**, 163903 (2015).

[5] C. Ernandes, H. J. Lin, M. Mortier, P. Gredin, M. Mivelle, and L. Aigouy, Exploring the magnetic and electric side of light through plasmonic nanocavities, Nano Lett. **18**, 5098 (2018).

[6] B. Choi, M. Iwanaga, Y. Sugimoto, K. Sakoda, and H. T. Miyazaki, Selective plasmonic enhancement of electric- and magnetic-dipole radiations of Er ions, Nano Lett. **16**, 5191 (2016).

[7] S. Murai, M. Saito, H. Sakamoto, M. Yamamoto, R. Kamakura, T. Nakanishi, K. Fujita, M. A. Verschuren, Y. Hasegawa, and K. Tanaka, Directional outcoupling of photoluminescence from Eu (III)-complex thin films by plasmonic array, APL Photonics **2**, 026104 (2017).

[8] R. Hussain, S. S. Kruk, C. E. Bonner, M. A. Noginov, I. Staude, Y. S. Kivshar, N. Noginova, and D. N. Neshev, Enhancing Eu^{3+} magnetic dipole emission by resonant plasmonic nanostructures, Opt. Lett. **40**, 1659 (2015).

[9] P. T. Worthing, R. M. Amos, and W. L. Barnes, Modification of the spontaneous emission rate of Eu^{3+} ions embedded within a dielectric layer above a silver mirror, Phys. Rev. A **59**, 865 (1999).

[10] A. I. Kuznetsov, A. E. Miroshnichenko, M. L. Brongersma, Y. S. Kivshar, and B. Luk'yanchuk, Optically resonant dielectric nanostructures, Science **354**, 2742 (2016).

[11] G. Videen and W. S. Bickel, Light-scattering resonances in small spheres, Phys. Rev. A **45**, 6008 (1992).

[12] J. W. Choong, N. Nefedkin, and A. Krasnok, Collectively driven optical nanoantennas, Phys. Rev. A **103**, 043714 (2021).

[13] Y. Cho, J. H. Huh, K. J. Park, K. Kim, J. Lee, and S. Lee, Using highly uniform and smooth selenium colloids as low-loss magnetodielectric building blocks of optical metafluids, Opt. Express **25**, 13822 (2017).

[14] M. K. Schmidt, R. Esteban, J. J. Sáenz, I. Suárez-Lacalle, S. Mackowski, and J. Aizpurua, Dielectric antennas—a suitable platform for controlling magnetic dipolar emission, Opt. Express **20**, 13636 (2012).

[15] G. C. Li, J. Xiang, Y. L. Zhang, F. Deng, M. Panmai, W. Zhuang, S. Lan, and D. Lei, Mapping the magnetic field intensity of light with the nonlinear optical emission of a silicon nanoparticle, Nano Lett. **21**, 2453 (2021).

[16] J. A. Parker, H. Sugimoto, B. Coe, D. Eggena, M. Fujii, N. F. Scherer, S. K. Gray, and U. Manna, Excitation of nonradiating anapoles in dielectric nanospheres, Phys. Rev. Lett. **124**, 097402 (2020).

[17] A. Vaskin, S. Mashhadi, M. Steinert, K. E. Chong, D. Keene, S. Nanz, A. Abass, E. Rusak, D. Y. Choi, I. Fernandez-Corbaton, T. Pertsch, C. Rockstuhl, M. A. Noginov, Y. S. Kivshar, D. N. Neshev, N. Noginova, and I. Staude, Manipulation of magnetic dipole emission from Eu^{3+} with Mie-resonant dielectric metasurfaces, Nano Lett. **19**, 1015 (2019).

[18] B. Rolly, B. Bebey, S. Bidault, B. Stout, and N. Bonod, Promoting magnetic dipolar transition in trivalent lanthanide ions with lossless Mie resonances, Phys. Rev. B **85**, 245432 (2012).

[19] H. Sugimoto and M. Fujii, Magnetic Purcell enhancement by magnetic quadrupole resonance of dielectric nanosphere antenna, ACS Photonics **8**, 1794 (2021).

[20] C. Tserkezis, R. Esteban, D. O. Sigle, J. Mertens, L. O. Herrmann, J. J. Baumberg, and J. Aizpurua, Hybridization of plasmonic antenna and cavity modes: Extreme optics of nanoparticle-on-mirror nanogaps, Phys. Rev. A **92**, 053811 (2015).

[21] G. M. Akselrod, C. Argyropoulos, T. B. Hoang, C. Ciracì, C. Fang, J. Huang, D. R. Smith, and M. H. Mikkelsen, Probing the mechanisms of large Purcell enhancement in plasmonic nanoantennas, Nat. Photonics **8**, 835 (2014).

[22] Z. Li, Q. You, H. Wang, L. Zhang, D. Zhang, S. Jia, Y. Fang, and P. Wang, Nanowire dimer optical antenna brightens the surface defects of silicon, Nanophotonics **12**, 1723 (2023).

[23] Z. Li, Q. You, J. Li, C. Zhu, L. Zhang, L. Yang, Y. Fang, and P. Wang, Boosting light–matter interaction in a longitudinal bonding dipole plasmon hybrid anapole system, J. Phys. Chem. C **127**, 3594 (2023).

[24] Y. Li, X. Bi, Q. You, Z. Li, L. Zhang, Y. Fang, and P. Wang, Strong coupling with directional scattering features of metal nanoshells with monolayer WS_2 heterostructures, Appl. Phys. Lett. **121**, 021140 (2022).

[25] K. J. Russell, K. Y. M. Yeung, and E. Hu, Measuring the mode volume of plasmonic nanocavities using coupled optical emitters, Phys. Rev. B **85**, 245445 (2012).

[26] S. Shen, L. Meng, Y. Zhang, J. Han, Z. Ma, S. Hu, Y. He, J. Li, B. Ren, T. M. Shih, Z. Wang, Z. Yang, and Z. Tian, Plasmon-enhanced second-harmonic generation nanorulers with ultrahigh sensitivities, Nano Lett. **15**, 6716 (2015).

[27] S. Chen, L. Y. Meng, H. Y. Shan, J. F. Li, L. Qian, C. T. Williams, Z. L. Yang, and Z. Q. Tian, How to light special hot spots in multiparticle-film configurations, ACS Nano **10**, 581 (2016).

[28] S. Chen, Y. Zhang, T. M. Shih, W. Yang, S. Hu, X. Hu, J. Li, B. Ren, B. Mao, Z. Yang, and Z. Tian, Plasmon-induced magnetic resonance enhanced Raman spectroscopy, Nano Lett. **18**, 2209 (2018).

[29] J. Wang, W. Yang, P. M. Radjenovic, Y. He, Z. Yang, and J. F. Li, Strong coupling between magnetic resonance and propagating surface plasmons at visible light frequencies, J. Chem. Phys. **152**, 014702 (2020).

[30] Y. Meng, Q. Zhang, D. Lei, Y. Li, S. Li, Z. Liu, W. Xie, and C. W. Leung, Plasmon-induced optical magnetism in an ultrathin metal nanosphere-based dimer-on-film nanocavity, Laser Photonics Rev. **14**, 2000068 (2020).

[31] B. Luk'yanchuk, N. I. Zheludev, S. A. Maier, N. J. Halas, P. Nordlander, H. Giessen, and C. T. Chong, The Fano resonance in plasmonic nanostructures and metamaterials, Nat. Mater. **9**, 707 (2010).

[32] Y. Bao, Z. Hu, Z. Li, X. Zhu, and Z. Fang, Magnetic plasmonic Fano resonance at optical frequency, Small **11**, 2177 (2015).

[33] J. A. Fan, K. Bao, C. Wu, J. Bao, R. Bardhan, N. J. Halas, V. N. Manoharan, G. Shvets, P. Nordlander, and F. Capasso, Fano-like interference in self-assembled plasmonic quadrumer clusters, Nano Lett. **10**, 4680 (2010).

[34] N. Verellen, Y. Sonnefraud, H. Sobhani, F. Hao, V. V. Moshchalkov, P. V. Dorpe, P. Nordlander, and S. A. Maier, Fano resonances in individual coherent plasmonic nanocavities, Nano Lett. **9**, 1663 (2009).

[35] Y. Francescato, V. Giannini, and S. A. Maier, Plasmonic systems unveiled by Fano resonances, ACS Nano **6**, 1830 (2012).

[36] E. M. Roller, L. K. Khorashad, M. Fedoruk, R. Schreiber, A. O. Govorov, and T. Liedl, DNA-assembled nanoparticle rings exhibit electric and magnetic resonances at visible frequencies, Nano Lett. **15**, 1368 (2015).

[37] T. Feng, W. Zhang, Z. Liang, Y. Xu, and A. E. Miroshnichenko, Isotropic magnetic Purcell effect, ACS Photonics **5**, 678 (2017).

[38] F. Shafiei, F. Monticone, K. Q. Le, X. X. Liu, T. Hartsfield, A. Alu, and X. Li, A subwavelength plasmonic metamolecule exhibiting magnetic-based optical Fano resonance, Nat. Nanotechnol. **8**, 95 (2013).

[39] A. Nazir, S. Panaro, R. Proietti Zaccaria, C. Liberale, F. De Angelis, and A. Toma, Fano coil-type resonance for magnetic hot-spot generation, Nano Lett. **14**, 3166 (2014).

[40] T. M. Nguyen *et al.*, Ultralow-loss substrate for nanophotonic dark-field microscopy, Nano Lett. **23**, 1546 (2023).

[41] A. Alù and N. Engheta, Dynamical theory of artificial optical magnetism produced by rings of plasmonic nanoparticles, Phys. Rev. B **78**, 085112 (2008).

[42] G. C. Li, D. Lei, M. Qiu, W. Jin, S. Lan, and A. V. Zayats, Light-induced symmetry breaking for enhancing second-harmonic generation from an ultrathin plasmonic nanocavity, Nat. Commun. **12**, 4326 (2021).

[43] R. Alaee, C. Rockstuhl, and I. Fernandez-Corbaton, An electromagnetic multipole expansion beyond the long-wavelength approximation, Opt. Commun. **407**, 17 (2018).

[44] A. B. Evlyukhin, T. Fischer, C. Reinhardt, and B. N. Chichkov, Optical theorem and multipole scattering of light by arbitrarily shaped nanoparticles, Phys. Rev. B **94**, 205434 (2016).

[45] S. Shen, Y. Wu, Y. Li, P. Xie, Q. Ding, X. Kuang, W. Wang, and W. Wang, Tuning magnetic Mie-exciton interaction from the intermediate to strong coupling regime in a WSe_2 monolayer coupled with dielectric-metal nanoresonators, Phys. Rev. B **105**, 155403 (2022).

[46] T. Yezekyan, V. A. Zenin, J. Beermann, and S. I. Bozhevolnyi, Anapole states in gap-surface plasmon resonators, Nano Lett. **22**, 6098 (2022).

[47] E. E. Radescu and G. Vaman, Exact calculation of the angular momentum loss, recoil force, and radiation intensity for an arbitrary source in terms of electric, magnetic, and toroid multipoles, Phys. Rev. E **65**, 046609 (2002).

[48] J. J. Choquette, K.-P. Marzlin, and B. C. Sanders, Superradiance, subradiance, and suppressed superradiance of dipoles near a metal interface, Phys. Rev. A **82**, 023827 (2010).

[49] Q. You, C. Zhang, Y. Wang, X. Bi, Z. Li, L. Zhang, D. Zhang, Y. Fang, and P. Wang, Biexcitons-plasmon coupling of Ag@Au hollow nanocube/MoS_2 heterostructures based on scattering spectra, Opt. Express **32**, 9105 (2024).

[50] P. B. Johnson and R. W. Christy, Optical constants of the noble metals, Phys. Rev. B **6**, 4370 (1972).

[51] E. M. Purcell, Spontaneous emission probabilities at radio frequencies, Phys. Rev. **69**, 681 (1946).

[52] S. M. Hein and H. Giessen, Tailoring magnetic dipole emission with plasmonic split-ring resonators, Phys. Rev. Lett. **111**, 026803 (2013).

[53] H.-W. Wu, Y. Li, H.-J. Chen, Z.-Q. Sheng, H. Jing, R.-H. Fan, and R.-W. Peng, Strong Purcell effect for terahertz magnetic dipole emission with spoof plasmonic structure, ACS Appl. Nano Mater. **2**, 1045 (2019).

[54] F. Kaminski, V. Sandoghdar, and M. Agio, Finite-difference time-domain modeling of decay rates in the near field of metal nanostructures, J. Comput. Theor. Nanosci. **4**, 635 (2007).